

Rail-gap switch with a multistep high-voltage triggering system

Cite as: Rev. Sci. Instrum. **91**, 114703 (2020); <https://doi.org/10.1063/5.0015104>

Submitted: 25 May 2020 . Accepted: 21 October 2020 . Published Online: 09 November 2020

 **Po-Yu Chang** (張博宇), **Chih-Jui Hsieh** (謝知毅), **Mei-Feng Huang** (黃梅鳳),  **Ming-Cheng Jheng** (鄭名城), **Yen-Cheng Lin** (林彥呈), **Jia-Kai Liu** (劉嘉楷), and **Sheng-Hua Yang** (楊昇樺)





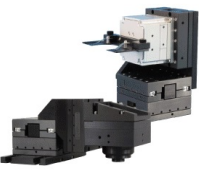
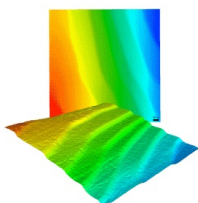
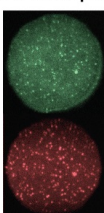
View Online



Export Citation



CrossMark

 MCL MAD CITY LABS INC. www.madcitylabs.com	<p>Nanopositioning Systems</p> 	<p>Modular Motion Control</p> 	<p>AFM and NSOM Instruments</p> 	<p>Single Molecule Microscopes</p> 
---	--	--	---	--

Rail-gap switch with a multistep high-voltage triggering system

Cite as: Rev. Sci. Instrum. 91, 114703 (2020); doi: 10.1063/5.0015104

Submitted: 25 May 2020 • Accepted: 21 October 2020 •

Published Online: 9 November 2020



Po-Yu Chang (張博宇),^{1,a)} Chih-Jui Hsieh (謝知叡),¹ Mei-Feng Huang (黃梅鳳),¹ Ming-Cheng Jheng (鄭名城),^{1,2} Yen-Cheng Lin (林彥呈),¹ Jia-Kai Liu (劉嘉楷),¹ and Sheng-Hua Yang (楊昇樺)¹

AFFILIATIONS

¹Institute of Space and Plasma Sciences, National Cheng Kung University, Tainan City 70101, Taiwan

²National Synchrotron Radiation Research Center (NSRRC), Hsinchu City 30076, Taiwan

^{a)} Author to whom correspondence should be addressed: pchang@mail.ncku.edu.tw

ABSTRACT

A rail-gap switch with a multistep triggering system was developed. The rail-gap switch consisted of two rail-like electrodes and a knife-edge electrode parallel to each other. It was assembled from many pieces and filled with unpressurized-flowing dry air. Good alignments between all electrodes were achieved by using a special jig and the knife-edge electrode as the spatial reference. Furthermore, to trigger the rail-gap switch, a multistep triggering system was used. The triggering system consisted of three components: an optical trigger-pulse generator, a slow high-voltage trigger-pulse generator using an ignition coil for a car, and finally, a fast high-voltage trigger-pulse generator using a three-stage Marx generator. The triggering system generated a negative high-voltage trigger pulse of less than -40 kV with a falling speed of -6.6 ± 0.4 kV/ns. The falling speed was fast enough to initiate multichannel discharges in the rail-gap switch. Finally, the rail-gap switch was tested using a test bench consisting of a 0.5 - μ F capacitor bank charged to 20 kV. The rail-gap switch was triggered by the multistep triggering system robustly with a delay of 180 ns. The delay between the time, when the peak current of the test bench occurred, and the trigger pulse was 890 ns with a jitter of 20 ns, i.e., $\sim 2\%$ uncertainty in time. The inductance of the rail-gap switch was ~ 80 nH obtained from the discharge tests. The rail-gap switch with the multistep high-voltage triggering system is suitable for any pulsed-power systems with current rise times in the order of 1 μ s.

Published under license by AIP Publishing. <https://doi.org/10.1063/5.0015104>

I. INTRODUCTION

Pulsed-power generators have many applications such as studies in plasma physics, nuclear fusion energy,^{1–4} radiation physics,^{4–6} high-energy-density physics,⁷ laboratory astrophysics,⁸ pinches,^{9,10} and so on. In a pulsed-power generator, energy is first stored capacitively, inductively, or mechanically. The energy is suddenly released so that pulsed-high power is provided. In most of the pulsed-power systems, capacitive storage is used due to the simplicity compared to other methods. The main components of a pulsed-power generator using capacitive storage are [high-voltage (HV)] capacitors and one or many closing switches. There are several key parameters that need to be considered for choosing a switch. They are as follows:¹¹

1. Working voltage: the switch needs to hold the voltage before it is activated.
2. Peak current: in order to have a high power output, a high current output is needed. It is the maximum current that can pass through the switch without damaging it.
3. Rising speed of the output current: it describes how long it takes for the current to rise to the peak value. It is also quantified as dI/dt .
4. Switch recovery time: it is the time it takes for a switch to be able to hold the working voltage after each discharge. For a system that needs to be discharged repetitively with a high frequency, the recovery time needs to be short.
5. Delay time: the time difference between the time the trigger pulse is delivered and the time the current starts to flow.
6. Jitter: the uncertainty in time that the current starts to flow after a trigger pulse is delivered.
7. Geometry: in order to fit the switch in the system, a particular switch may be used even if it has the similar performance with other kinds of switches.

The most common high-voltage switch is a spark-gap switch, which is a pair of electrodes with a gap in between, as shown in Fig. 1(a). The working voltage mainly depends on the gap distance

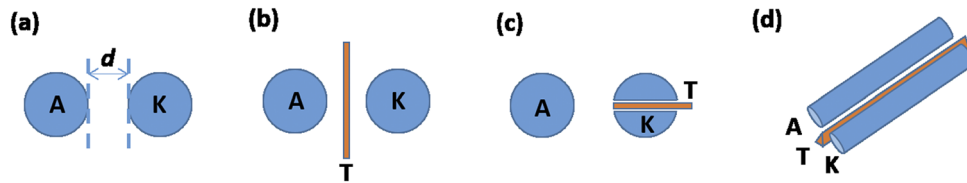


FIG. 1. (a) A spark-gap switch. (b) A three-electrode spark-gap switch. (c) A trigatron. (d) A rail-gap switch. All electrodes labeled as “A” are anodes, while all electrodes labeled as “K” are cathodes. All electrodes labeled as “T” are triggering electrodes.

d , the type, and the pressure of the filled gas of the switch. The spark gap needs to hold the working voltage before it is activated. A breakdown between the electrodes needs to be initiated for activating the switch. The simplest way to initiate the breakdown is to disturb the electric field within the switch using a high-voltage trigger pulse delivered through the third electrode, such as the three-electrode spark-gap switch and the trigatron, as shown in Figs. 1(b) and 1(c). For example, assume that all electrodes labeled as “A” are connected to the positive high voltage as the anodes, while all electrodes labeled as “K” are connected to ground as the cathodes. To activate the switch, one just needs to deliver a negative high voltage to the electrodes labeled as “T” to initiate the breakdown in the switch.

To provide high power, the inductance of the pulsed-power system needs to be as low as possible. Moreover, all components need to be able to carry large currents during discharges. Among different closing switches, the multichannel discharge in a rail-gap switch provides a low inductance. On the other hand, long rail-like electrodes can handle large currents. Therefore, a rail-gap switch,^{12–16} as shown in Fig. 1(d), is one of the options for carrying high currents and high power. Furthermore, if the pulse current will be delivered to a load through a parallel-plate transmission line (PPTL), the rail-gap switch fits with the PPTL better since it can be directly connected to one of the plates of the PPTL without shrinking the width of the transmission line. Considering the geometric factor, a rail-gap switch is also more beneficial compared to other kinds of spark-gap switches for PPTL.

The rail-gap switch consists of two rail-like electrodes and a knife-edge electrode. There are two challenges to make the rail-gap switch. The first challenge is that all electrodes need to be parallel to each other. Therefore, the electric field is distributed uniformly along the electrodes in both cases: (1) when the switch is open and (2) when it is closed due to overvoltage between the gaps. If all electrodes are not perfectly parallel to each other, a single discharge channel may occur at the location with the shortest gap distance. On the other hand, a single plastic piece such as epoxy is used as the switch body in most rail-gap switches to date for holding high voltages. It is not easy to fabricate the whole body in one piece. Most importantly, plastic is generally softer than metal so that it is less accurate in machining. In this paper, the rail-gap switch was designed such that it was assembled by many small pieces. It reduced the difficulty in machining dramatically. To align all electrodes relative to each other, one of the electrodes was used as the reference. The other two electrodes were then mounted relative to the reference electrode using a special jig. Therefore, good alignments between all electrodes are achieved. The second challenge is that multichannel discharges can

only be initiated when a high-voltage (HV) trigger pulse with a rising or falling speed higher than 5 kV/ns ¹² is provided. It is to ensure that a multichannel is formed before the voltage across the main gap drops significantly. One way to generate a fast HV trigger pulse is using a transmission line transformer (TLT).¹⁷ The advantage of the TLT is that it can activate a rail-gap switch reliably with a low jitter. However, long coaxial cables that occupy a lot of space are needed for the TLT. Here, in this paper, a multistep high-voltage triggering system consisting of a three-stage Marx generator was used. The Marx generator was much more compact than the TLT.

This paper is arranged as follows: in Sec. II, the design and the simulated electric fields of the rail-gap switch are given; in Sec. III, the multistep triggering system is introduced. The design and the performance of each step and the final trigger pulse are given; in Sec. IV, the discharge test of the rail-gap switch triggered by the multistep triggering system is presented; finally, in Sec. V, a summary is given.

II. THE RAIL-GAP SWITCH

The rail-gap switch we built was assembled by many small pieces. Therefore, it was fabricated easily. To achieve good alignments between electrodes, a special jig was used. Designs of the rail-gap switch and the jig are first introduced. The simulated electric potentials and electric fields are then given.

A. Design of the rail-gap switch

1. The rail-gap switch

The rail-gap switch consists of two rail-like electrodes and a knife-edge electrode, as shown in Fig. 2. All electrodes are made of stainless steel 304. In the future, we will use brass instead of stainless steel due to its higher thermal and electrical conductivity. The rail-like electrodes are cylinders with a diameter of 50 mm. The edges of the cylinder are rounded with the same radius. The total length of the cylinder, including the rounded part, is 300 mm. In between, the third electrode with a knife edge on the top called the knife-edge electrode is used as the triggering electrode. The corners of two ends of the knife-edge electrode are rounded with a radius of 2 mm. The knife-edge angle is 30° with a rounded radius of 0.5 mm. The tip of the knife-edge electrode is 10 mm lower than the center of the rail-like electrodes. The center plane of the knife-edge electrode is located at about one-third of the gap between two rail-like electrodes. Initially, the gap distance between two rail-like electrodes was 9 mm in total. In other words, the distances between the knife-edge

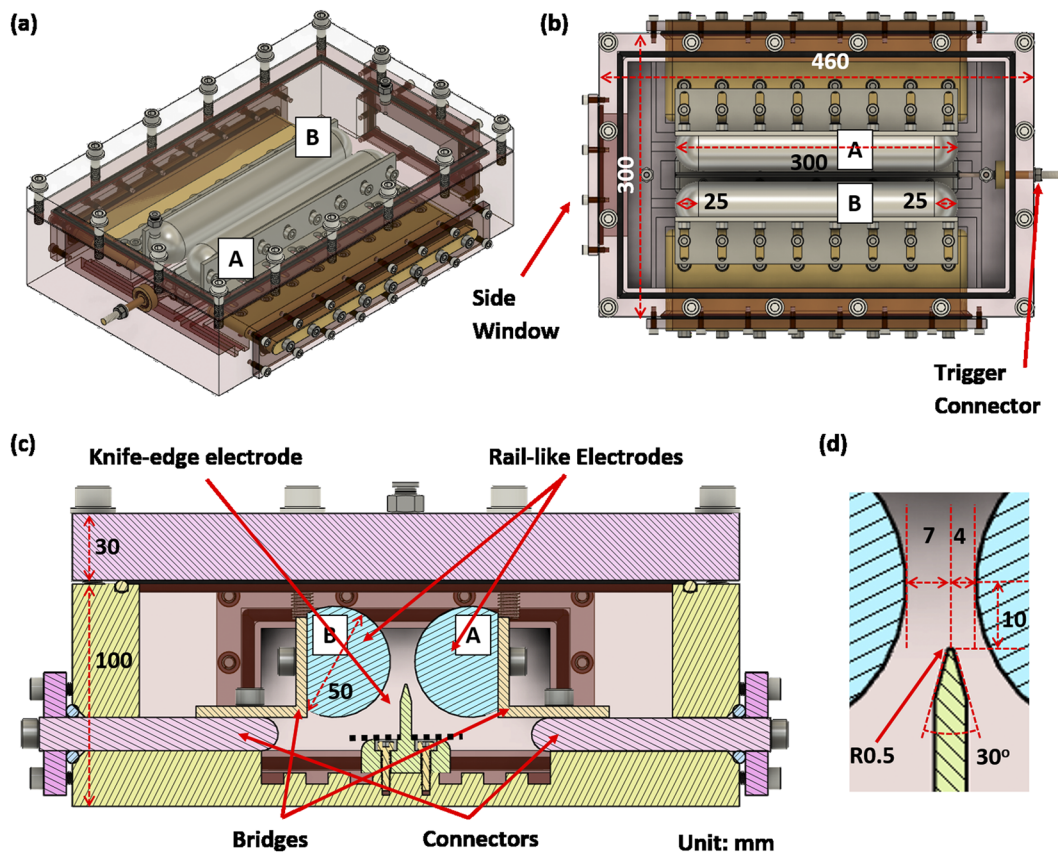


FIG. 2. (a) The computer-aided design (CAD) drawing of our rail-gap switches. (b) and (c) are the top view and the cross section of the rail-gap switch, respectively. The black-dashed line in (c) is the spatial reference for all electrodes. (d) The enlarged view of the tip of the knife-edge electrode. Courtesy of Ref. 18. Reprinted with permission from M.-C. Jheng, "Development of a 400 MW pulsed-power system," M.Sc. thesis, National Cheng Kung University, 2019.

electrode and each rail-like electrode were 3 mm and 6 mm, respectively. In this case, the self-breakdown voltage was 29.4 ± 0.9 kV.¹⁸ To have a robust operation, we added 1 mm to each gap between the knife-edge electrode and each rail-like electrode, i.e., 4 mm and 7 mm, respectively, as shown in Fig. 2. In order to show that the rail-gap switch is capable for a higher working voltage, we have tested the self-breakdown voltage with the gap distance of 7 mm and 14 mm, i.e., 21 mm in total. The breakdown voltage was 42 ± 3 kV.¹⁹ The breakdown voltage is almost linearly proportional to the product of gas pressure and the gap distance at a large gap distance and high pressure. We expect that the working voltage can be even higher for a larger gap distance and higher filled-gas pressure. Nevertheless, the gap distance between two rail-like electrodes was 11 mm in total and was used throughout this paper.

When the rail-gap switch is used, the rail-like electrode closer to the knife-edge electrode labeled as "A" is at ground, while the one, further, away from the knife-edge electrode labeled as "B" is at 20 kV. Before the rail-gap switch is activated, a resistor divider, consisting of one 2-G Ω resistor and one 1-G Ω resistor connected in series, is used to keep the potential of the knife-edge electrode at ~ 6.7 kV, i.e., about one-third of 20 kV. To activate the rail-gap switch, a negative

high-voltage trigger pulse with a peak voltage less than -40 kV is sent to the knife-edge electrode.

We use polyoxymethylene (POM) for the body due to its excellent mechanical strength, abrasion, fatigue resistance, and moldability. It is different from epoxy, which is used in most rail-gap switches. However, POM is not particularly UV resistant. It may need to be replaced after some time. The cover is made of acrylic so that we can observe the activation of the switch. There are some grooves at the bottom of the body, as shown in Fig. 2. They are made to prevent flashover across the bottom surface. The filled gas of the rail-gap switch is dry air provided by a compressed gas cylinder for medical uses. The dew point temperature of the dry air is -40°C , i.e., the relative humidity at 20°C is less than 1%. Although the rail-gap switch is capable of holding pressurized gas and, thus, higher voltage, it is not pressurized so far. Instead, we keep the dry air flowing through the box with a flow rate of 8 l/min so that the air is fresh and well controlled between experiments.

At the side of the rail-gap switch body, there is a side window made of acrylic. It can be used to observe the discharge between electrodes. Most importantly, it is used to take out the jig we used to control the spacing between all electrodes, which will be

introduced in Sec. II A 2. The spatial reference of distances between all electrodes is the top surface of the foot of the knife-edge electrode indicated by the black-dashed line in Fig. 2(c). Therefore, the jig is between all electrodes when we set up the distance between them. In other words, it is not possible to take out the jig from the top. Thus, the window at the side of the box is important so that the jig can be removed after all electrodes are mounted.

2. The jig

The spatial reference of distances between all electrodes is the top surface of the foot of the knife-edge electrode indicated by the black-dashed line in Fig. 2(c). It is to avoid the inaccuracy when all components are manufactured separately. Particularly, the box is made of plastic that is softer than electrodes made of metal so that the tolerance is much lower. In other words, it is not possible to use the box as the spatial reference. Shown in Figs. 3(a) and 3(c) are the top view and the bottom view of the special jig we built to control the spacing between electrodes. There is a groove at the bottom of the jig, as shown in Fig. 3(c). The width of the groove is the same as the width of the knife-edge electrode. Therefore, the jig is put on top of the pre-installed knife-edge electrode as the spatial reference. The jig was assembled from many rectangular metal plates made of stainless steel 304 with precisely machined thickness with an accuracy of 10 μm . The accuracy was confirmed by using a micrometer caliper. For those rectangular metal plates, they did not deform after they were made. However, for those asymmetric parts, they bowed if they were not machined carefully. Therefore, the machining went through few steps. The first time when they were machined, only rough cuts were made. Then, the machinist let it bow for few days. Afterward, more cuts would be made. The processes were repeated many times until they met the tolerance requirements. The length of the cylindrical part of the rail-like electrode is 250 mm. In other words, all electrodes are parallel to each other within an angle of $\pm 5 \times 10^{-3}$ deg. To generate multichannel discharges, the gap needs to be overvolted uniformly and each channel needs to be formed before the voltage across the gap drops significantly. The jitter of closing a channel must be in the order of one-tenth of the falling time of the voltage across the gap.^{17,20,21} The jitter in percentage is about the variation of the gap distance. In other words, the accuracy in machining we have is way more than enough to obtain the multichannel. Nevertheless, we still had all parts made with the accuracy.

To have the flexibility for the rail-gap switch being operated in different voltages, the width of the jig can be adjusted by changing

the thickness of the central plate indicated by the red circle in Fig. 3(c). To adjust the positions of all electrodes, the knife-edge electrode is first mounted on the box. The jig is then put on top of the knife-edge electrode such that the electrode is in the groove of the jig, as shown in Fig. 3(b). Afterward, the rail-like electrodes are mounted on the box with the position relative to the knife-edge electrode with a fixed distance using the jig indicated as the red-dashed line in Fig. 3(b). Finally, the jig can be taken out through the side window of the body.

B. Simulations of electric fields

The breakdown electric field for dry air at the standard atmospheric condition is ~ 3 MV/m.²² Although the breakdown voltage may occur below 3 MV/m, we would like to use it as a guideline for understanding how the electric field distributed in the rail-gap switch in simulations. The actual gap distance will be adjusted and determined in experiments. Before the rail-gap switch is activated, the electric field needs to be lower than the breakdown electric field. On the contrary, the electric field needs to be higher than the breakdown electric field when the rail-gap switch is triggered. Therefore, we confirmed that the electric field strength met the requirements in simulations with the actual geometry of the rail-gap switch. The electric potential was first calculated by solving Poisson's equation numerically using COMSOL Multiphysics^{®23} by setting the potential far away from the system at ground as the boundary condition. The electric field was then calculated by taking the gradient of the simulated electrical potential. Two cases were simulated: (1) before the rail-gap switch was activated where the potential of the knife-edge electrode was ~ 6.7 keV and (2) when the rail-gap switch was activated where the potential of the knife-edge electrode was -40 kV when the trigger pulse was sent to the electrode.

For any switches, they need to hold the voltage before being activated. A breakdown needs to be initiated when the trigger pulse is delivered so that the switches are activated. However, the switching time of the switch depends on four factors:¹¹ (1) the statistic delay time for generating free electrons t_s , (2) the streamer forming time t_f , (3) the channel heating time t_{heat} , and (4) the rising speed of the trigger pulse. Both factors t_f and t_{heat} are inversely proportional to the electric field. In other words, with higher overvoltage, the switch can be activated faster. On the other hand, to trigger the rail-gap switch with a low jitter, an HV trigger pulse with rising or falling speed higher than 5 kV/ns^{12,17} is required. The falling speed

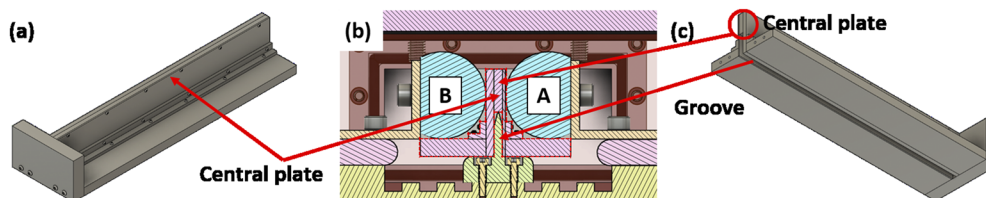


FIG. 3. (a) The top view of the CAD drawing of the jig. (b) The CAD drawing of the jig being used to determine the positions of electrodes relative to each other. (c) The bottom view of the CAD drawing of the jig. The jig pointed out by the red-dashed line can be slid out through the side window. The width of the jig can be adjusted by replacing the central plate with different thicknesses. Courtesy of Ref. 18. Reprinted with permission from M.-C. Jheng, "Development of a 400 MW pulsed-power system," M.Sc. thesis, National Cheng Kung University, 2019.

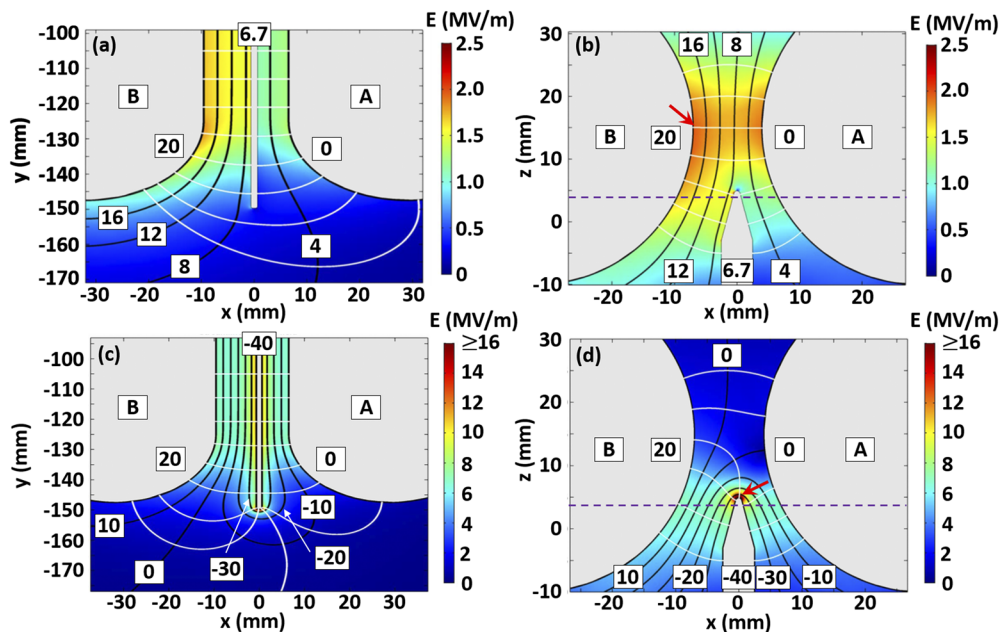


FIG. 4. In all figures, the contours are amplitudes of electric fields in MV/m; the black lines with labels are electric potentials in kV; the white lines are electric field lines; the gray areas are electrodes with the same labels in Figs. 2 and 3. (a) and (b) are the top view and the side view, respectively, for Case 1. (c) and (d) are the top view and the side view, respectively, for Case 2. (a) and (c) are from the cut plane 1 mm below the tip of the knife-edge electrode, the purple-dashed line in (b) and (d). The location of the maximum electric fields is pointed out by red arrows.

of our trigger pulse will be described in Sec. III. The simulation here is to ensure that the voltage is much below the breakdown voltage before the rail-gap switch is activated and significant overvoltage is applied to the knife-edge electrode for triggering the rail-gap switch.

Shown in Fig. 4 are the simulated results where black-solid lines with labels represent the electric potentials, the color contours are the strength of the electric fields, and the white lines are electric field lines. Figures 4(a) and 4(b) are the simulated results of Case 1, while (c) and (d) are for Case 2. Figures 4(a) and 4(c) are the top views of the cut plane 1 mm below the tip of the knife-edge electrode, the purple-dashed line in Figs. 4(b) and 4(d). Figures 4(b) and 4(d) are the side views of the cut plane right at the middle of the knife-edge electrode.

In Case 1, both the electric potential and the electric field strength are uniformly distributed along the rail-like electrodes, as shown in Fig. 4(a). Since the knife-edge electrode is longer than the rail-like electrodes, the electric field is weaker at the side of the knife-edge electrode. Therefore, the electrical breakdown at the side corner of the knife-edge electrode is prevented. On the other hand, from the side view given in Fig. 4(b), both the electric potential and the electric field strength are also uniformly distributed between two rail-like electrodes. They are slightly stronger between two rail-like electrodes than between each rail-like electrode and the knife-edge electrode. The maximum electric field is ~ 1.96 MV/m located at the center of the rail-like electrode indicated by the red arrow in Fig. 4(b). Most importantly, the electric field much less than 3 MV/m indicates that the rail-gap switch is capable of holding 20 kV, which coincides with the measured self-breakdown voltage. Nevertheless, the

electric field strength close to the required breakdown electric field indicates that a breakdown can be easily triggered by perturbing the electric field using an HV trigger pulse delivered to the knife-edge electrode.

In Case 2, both the electric potential and the electric field strength are also uniformly distributed along the rail-like electrode, as shown in Fig. 4(c). A strong electric field occurs at the side corner of the knife-edge electrode due to its sharp edge. Nevertheless, the electric field at the side corner is weaker than that at the tip of the knife-edge electrode and they are pointed toward neither of the rail-like electrodes. The electric field lines coming out from the side corner of the knife-edge electrode are much longer than those between the knife-edge electrode and each rail-like electrode. As a result, the breakdown does not always happen at the side corner. On the other hand, from the side view given in Fig. 4(d), a strong electric field occurs at the tip of the knife-edge electrode since the potential of the electrode is at -40 kV when the trigger pulse is delivered. The maximum electric field is ~ 21 MV/m located at the tip of the knife-edge electrode indicated by the red arrow in Fig. 4(d). The electric field between the knife-edge electrode and each rail-like electrode is much higher than 3 MV/m. In other words, a breakdown can occur, and thus, the rail-gap switch is activated.

III. THE MULTISTEP HIGH-VOLTAGE TRIGGERING SYSTEM

To trigger the rail-gap switch with a low jitter, an HV trigger pulse with rising or falling speed higher than 5 kV/ns^{12,17} is

required. A multistep triggering system is used to generate the HV trigger pulse that meets the requirement. The multistep triggering system consists of (A) an optical trigger-pulse generator, (B) a slow HV trigger-pulse generator, and (C) a fast HV trigger-pulse generator. The fast HV trigger-pulse generator is triggered by the slow HV trigger-pulse generator, which is triggered by the optical trigger-pulse generator. Three components and their performances are given in the following.

A. The optical trigger-pulse generator

The optical trigger-pulse generator is the initiator of all sequential events. A square pulse with a width of 1.25 ms needs to be generated for triggering the slow HV trigger-pulse generator described in Sec. III B. An Arduino-nano board is used as the main component of the trigger-pulse generator. The Arduino-nano board is suitable to generate the 1.25-ms pulse, which is not a very fast pulse. The board is preprogrammed to be controlled by switch buttons, to control LED indicators providing the information of different modes of the generator, and, most importantly, to provide the pulse. Shown in Fig. 5(a) is the circuit design of the generator. Two switches, one toggle switch as the safety and one push-button switch as the “Fire” button, are used. The generator has two modes: “Standby” mode and “Ready to Fire” mode. Shown in Fig. 5(b) is the flow chart of the status of the generator. The pulse can only be generated

when the **Fire** button is pressed, while the generator is in the **Ready to Fire** mode. Only when the toggle switch is switched from the OFF state to ON state, the system is transited to the **Ready to Fire** mode. In other words, the generator is in the **Standby** mode most of the time so that no pulse is generated even if the **Fire** button is pressed.

To prevent the electromagnetic pulse (EMP) from the downstream discharge from coming back through the electrical cable, an optical signal is used for insulation. Therefore, the square pulse generated by the Arduino-nano board is converted to an optical signal using a 10 Mb/s fiber optic transmitter (Avago HFBR-1528Z). The optical pulse with a wavelength of 650-nm (red) is then sent to the slow HV trigger-pulse generator through a plastic optical fiber (POF) cable. The POF cable is used as an EMP insulator between the optical trigger-pulse generator and the slow HV trigger-pulse generator.

B. The slow high-voltage trigger-pulse generator

We use a trigatron in the three-stage Marx generator, which will be introduced in Sec. III C. Therefore, we built a slow HV trigger-pulse generator to trigger the trigatron. The optical triggering signal introduced in Sec. III A is first converted to a ± 5 -V square pulse. Then, the slow HV trigger-pulse generator is controlled by the square pulse.

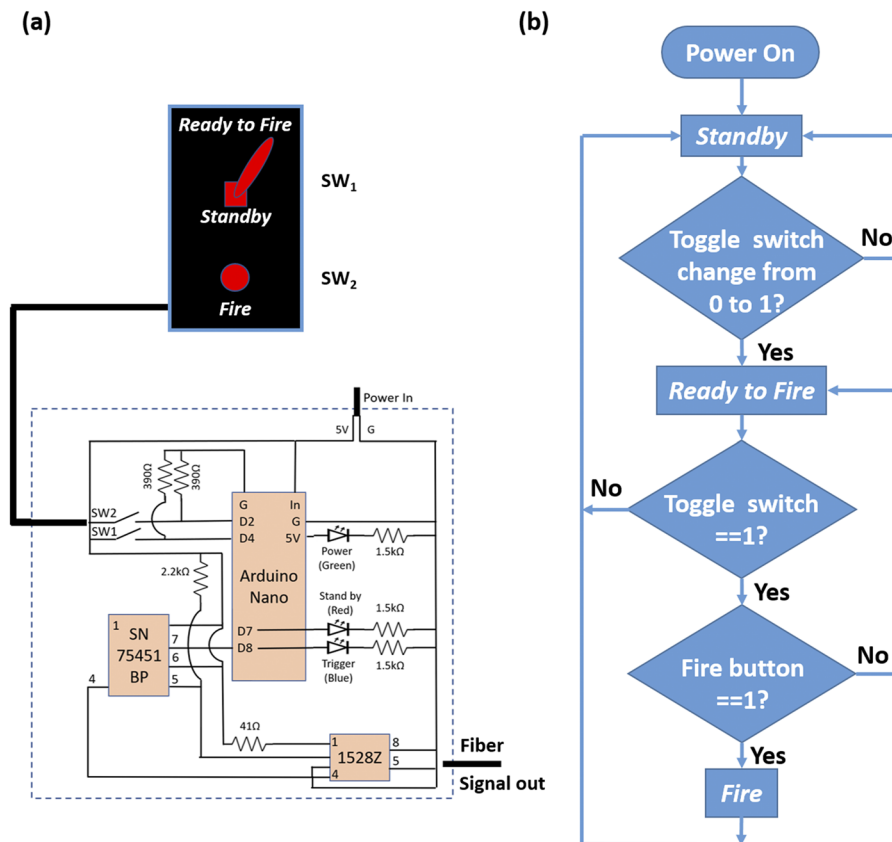


FIG. 5. (a) The circuit of the optical trigger-pulse generator. (b) The flow chart of the generator. The pulse can only be generated when the push button is pressed, while the generator is in the **Ready to Fire** mode.

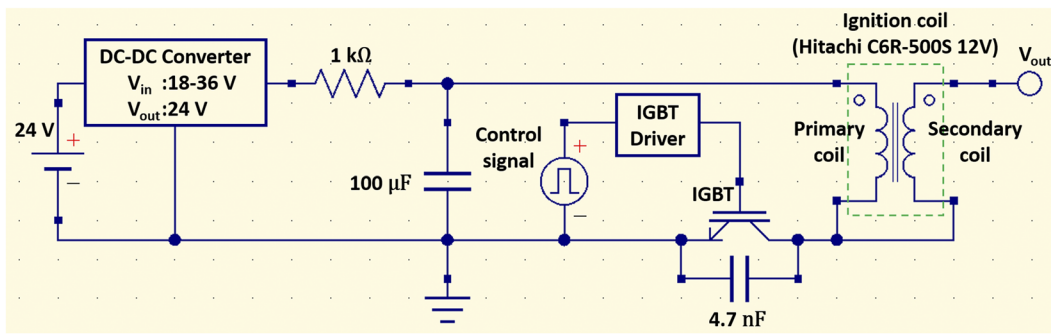


FIG. 6. Circuit of the slow HV trigger-pulse generator. Reproduced and reprinted with permission from M.-F. Huang, "Rust remover using small pulsed-power system," M.Sc. thesis, National Cheng Kung University, 2017.²⁵

1. The circuit design

To provide the HV pulse, the principle of the inductive energy storage is used. We use an ignition coil for a car (Hitachi C6R-500S 12V) as the main component of the slow HV trigger-pulse generator since the ignition coil for a car can store energy inductively and is very robust. Shown in Fig. 6 is the circuit of the slow HV trigger-pulse generator. Notice that to prevent any instruments get damaged by the EMP from the downstream discharge through power cables, we use a 24-V battery as the power source. A 24-V DC-DC converter provides a steady DC voltage. To convert the optical signal to the square pulse, an optical receiver (Avago HFBR-2528Z), which is not shown in Fig. 6, is used.²⁴ The primary coil of the ignition coil is the inductor that stores the energy for the high-voltage pulse. The 1-k Ω resistor is used to protect the 24-V DC-DC converter. The 100- μ F capacitor is first charged by the converter so that it can provide the output power. An Insulated Gate Bipolar Transistor (IGBT, Toshiba GT60M324) acts as a switch and is controlled by the square pulse with an amplitude of ± 15 V. The square pulse is converted from the ± 5 -V square pulse using an IGBT driver (Fairchild Semiconductor, FOD3184-V507D). The 4.7-nF capacitor is to protect the IGBT. When the IGBT is OFF, i.e., the circuit across the IGBT is open, the 100- μ F capacitor is charged to 24 V storing 28.8 mJ of energy. When the IGBT is ON, i.e., the circuit across the IGBT is closed, the current starts flowing from the 100- μ F capacitor through the primary coil of the ignition coil. The energy oscillates between the 100- μ F capacitor and the primary coil of the ignition coil. When the current reaches the maximum at 1.25 ms after the IGBT is ON, the IGBT is turned OFF so that the current is suddenly cut off. A voltage is then induced across the primary coil. As a result, a high voltage at the secondary coil is generated.

2. Output

As shown in Fig. 7, the blue line is the voltage output of the slow HV trigger-pulse generator V_{out} . The green line is the voltage across the 100- μ F capacitor V_{cap} . The red line is the ± 5 -V square pulse, which is the control signal $V_{control}$ that controls the IGBT through the IGBT driver. When the voltage of the square pulse was less than zero, the IGBT was OFF. Otherwise, the IGBT was ON. When the IGBT transits from OFF to ON at $t = 0$ s, the current started to flow through the primary coil. A voltage was induced across the primary coil during the status transition of the IGBT so that a high voltage

was induced at the secondary coil, i.e., a positive output voltage present at the output. It was not the HV output we needed. It could have been eliminated by slowing down the rising speed of the square pulse, i.e., a smaller dI/dt , or adding a diode at the output. However, since the positive HV output was not high enough to trigger the downstream trigatron, we did not bother to eliminate the small positive HV output. During the time that the IGBT was ON, the voltage across the capacitor dropped. Finally, the IGBT was turned OFF when the voltage across the capacitor dropped to near zero. A negative high voltage of less than -20 kV was then generated. After trial and error, the most negative HV voltage was provided when 1.25 ms was used as the width of the square pulse, even if V_{cap} did not drop to zero. The rise time of the HV pulse output defined as the time difference between the corner of the output voltage and -20 kV was 55.5μ s with a jitter of 0.4μ s defined as one standard deviation.

C. The fast high-voltage trigger-pulse generator

A small pulsed-power system is used to provide the fast HV trigger pulse. The falling speed of the output signal is restricted by the activating speed of the spark-gap switch. Instead of increasing the switching speed, the voltage of the trigger pulse is increased. In other words, higher voltage is provided with the same switching time so that a faster falling speed is provided. Therefore, to increase the output voltage, a three-stage Marx generator is used.

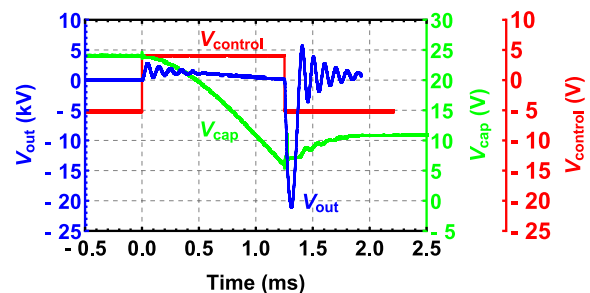


FIG. 7. Output of the slow HV trigger-pulse generator. The blue line is the output signal. The green line is the voltage of the 100- μ F capacitor. The red line is the control signal. Reproduced and reprinted with permission from M.-F. Huang, "Rust remover using small pulsed-power system," M.Sc. thesis, National Cheng Kung University, 2017.²⁵

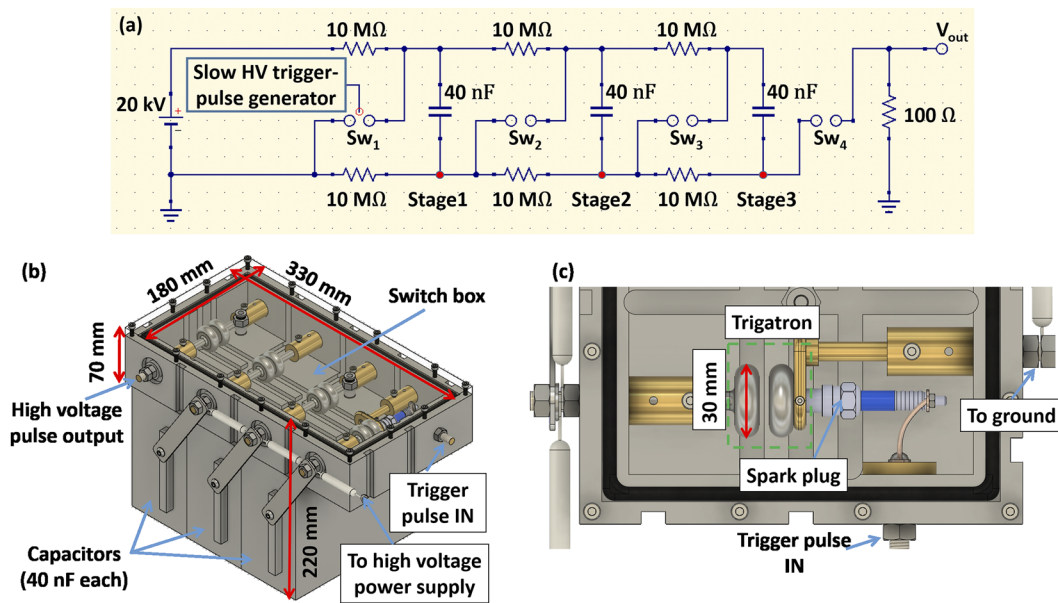


FIG. 8. (a) The circuit of the fast HV trigger-pulse generator. (b) The CAD drawing of the pulse generator. The switch box is placed on top of three HV capacitors. (c) The CAD drawing of the top view of the trigatron. Courtesy of Ref. 18. Reprinted with permission from M.-C. Jheng, “Development of a 400 MW pulsed-power system,” M.Sc. thesis, National Cheng Kung University, 2019.

1. The three-stage Marx generator

Shown in Fig. 8 is the design of the Marx generator. Three 40-nF capacitors made by Shanghai Pluspark Electronics Co., Ltd., China²⁶ are charged to 20 kV storing 24 J of energy. There are four spark-gap switches in the switch box. The switch box can be pressurized if a higher operating voltage is required. Nevertheless, the same dry air with the same flow rate as that used for the rail-gap switch is used. Therefore, the air in the switch box is fresh and well controlled between experiments. Electrodes in all switches are disk electrodes made of stainless steel 304 with 30 mm diameter, 10 mm thickness, and a rounded edge of 5 mm radius. The gap distance between two electrodes in each spark-gap switch is 10 mm. The first switch (Sw_1) is a trigatron so that the discharge is controlled. The rest of the switches (Sw_{2-4}) in the Marx generator are just self-breakdown spark-gap switches. The last switch (Sw_4) works as a peaking switch so that an HV pulse with the required falling speed is provided. The shape of the electrons of the trigatron is the same as those in the self-breakdown switches. The only difference between the trigatron and the self-breakdown switch is that a spark plug for a motorcycle is inserted to the center of the grounded electron of the trigatron as the triggering electrode. There are several advantages using the spark plug for a motorcycle: (a) it is a mature product with a long lifetime, (b) it provides good high-voltage insulation and gas seal between the triggering electrode and the ground electrode, (c) there are plenty of products off the shelf, and (d) it is easily triggered by an HV pulse generated by the ignition coil for a car introduced in Sec. III B. A 100- Ω resistor as the load is to ensure that the peaking switch is overvolted after all the other switches are closed. Finally, the high voltage across the resistor is generated for triggering the rail-gap switch.

2. Output

Shown in Fig. 9(a) is the output of the fast HV trigger-pulse generator. Although the peaking switch was used, two small voltage drops occurred before the main pulse was generated. Those two drops corresponded to Sw_1 and Sw_2 being activated, which will be discussed in detail in the following paragraph. The amplitudes of those two drops were not high enough to trigger the rail-gap switch. Moreover, the peaking switch was not activated yet so that the energy stored in the three-stage Marx generator was not delivered to the rail-gap switch for activating the rail-gap switch either. Therefore, we focused on the falling speed of the main pulse that dropped below -40 kV. We fitted the falling edge of the main pulse with a straight line, as indicated by the red-dashed line in Fig. 9(a). The slope of the fitted straight line, -6.6 ± 0.4 kV/ns, was the falling speed of the pulse. It met the requirement in falling speed for triggering a rail-gap switch with multichannel discharges.

To show that those two drops in Fig. 9(a) corresponded to Sw_1 and Sw_2 being activated, voltages at the first and the second stage of the three-stage Marx generator marked as red dots and labeled as “Stage1” and “Stage2” in Fig. 8(a) were measured and shown in Fig. 9(b). The output of the three-stage Marx generator, V_{out} , is also shown in Fig. 9(b). The data of “Stage2” and “ V_{out} ” were from the same shot, while the data of “Stage1” were from a different shot. Thus, the timing was slightly off between the lines of “Stage1” and “Stage2”. To show the phenomenon more clearly, M8 cap nuts were used as electrodes in all spark-gap switches except the first switch, i.e., the trigatron. Therefore, the delay time between those two drops was longer than that in Fig. 9(a), but the physics was the same. As expected, the voltage of each stage dropped in steps as the switch in each stage was closed. It is very clear that those two

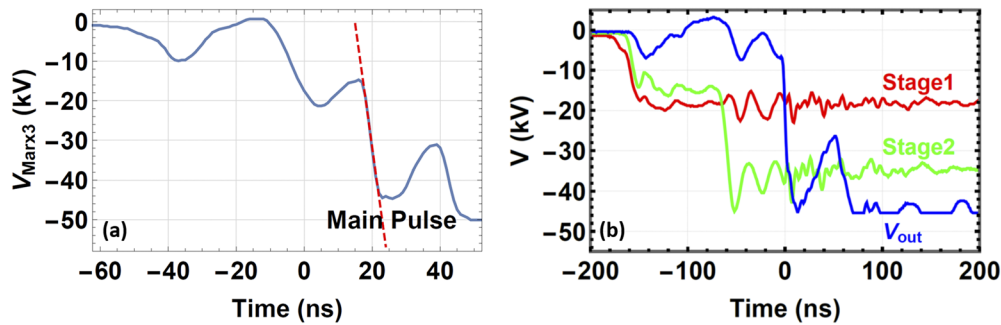


FIG. 9. (a) The output of the fast HV trigger-pulse generator. The falling speed, which is the slope of the red-dashed line, is -6.6 ± 0.4 kV/ns. Reproduced and reprinted with permission from M.-C. Jheng, "Development of a 400 MW pulsed-power system," M.Sc. thesis, National Cheng Kung University, 2019.¹⁸ (b) The voltage at the first stage in red, the second stage in green, and the output of the three-stage Marx generator in blue.

drops of V_{out} occurred at the same time as the voltage of Stage1 and Stage2 dropped. The reason for the small drops occurred at V_{out} is the following. Any switches are like capacitors before they are closed. When no switches were activated, no voltage was across Sw_4 . When Sw_1 was activated, the voltage at Stage1 dropped to -20 kV. Only small currents flew through each $10\text{-M}\Omega$ resistor. In other words, voltages at Stage1 to Stage3 all dropped to ~ -20 kV, as shown in Fig. 9(b). At this moment, Sw_4 was not activated and acted as a capacitor without being charged. In other words, the voltage across Sw_4 remained zero so that the voltage at V_{out} also tended to drop as Sw_1 was being activated. However, Sw_4 as a capacitor was being charged through the $100\text{-}\Omega$ resistor when the voltage at Stage3 started dropping. The voltage across Sw_4 eventually charged to ~ 20 kV. In other words, the voltage V_{out} went back to zero after some time. Similarly, the same process happened when Sw_2 was being activated. Therefore, there were two small voltage drops before the main pulse was generated. How fast the small drops went back to zero depended on how fast the effective capacitor across Sw_4 was charged through the $100\text{-}\Omega$ resistor. Therefore, it would depend on the resistance of the load that was $100\text{-}\Omega$ in Fig. 8(a) and the capacitance depended on the geometry of the peaking switch Sw_4 .

We have tested the performance of using $1\text{ k}\Omega$, $100\text{ }\Omega$, and $50\text{ }\Omega$ as the load resistor. For a larger load resistor, it took longer time to charge the effective capacitance across Sw_4 . Therefore, it took longer time for two small drops to go back to zero for using the $1\text{-k}\Omega$ resistor as the load. The time differences between each switch being activated were also longer. On the other hand, we did not see a significant difference between using the $100\text{-}\Omega$ and $50\text{-}\Omega$ resistors. Therefore, the $100\text{-}\Omega$ resistor was chosen.

IV. DISCHARGE TEST OF THE RAIL-GAP SWITCH

A test bench, which is shown in Fig. 10, was built to test the discharge of the rail-gap switch and the triggering system. In the system, two double-ended capacitors made by Yuhchang Electric Co., Ltd., Taiwan²⁷ with a capacitance of $1\text{ }\mu\text{F}$ were connected in series using an aluminum plate with a width of 100 mm and a thickness of 1.5 mm . In other words, the total capacitance of the system was $0.5\text{ }\mu\text{F}$. The rail-gap switch was placed on top of the capacitors. A

current monitor (Pearson model 301 \times) was placed in between the capacitors and the switch. Two AWG16 high-voltage silicone wires with 50 tinned-copper cores and 100 mm length were used to connect between each end of the capacitors and each electrode of the rail-gap switch. Those two wires connected between the grounded end of the capacitor and the rail-gap switch (electrode A in Fig. 2) went through the center of the current monitor so that the discharge currents were measured. The voltage of the capacitors, i.e., the voltage across the rail-gap switch, was also measured using an oscilloscope (Tektronix TDS 2024) via a 1000 to 1 high-voltage probe (Tektronix P6015A). The system was charged to 20 kV . The knife-edge electrode was connected to the output of the multistep triggering system through a 40 pF capacitor. A resistive voltage divider using a $2\text{-G}\Omega$ resistor and a $1\text{-G}\Omega$ resistor connected in series was used to keep the potential of the knife-edge electrode at $\sim 6.7\text{ kV}$ when the capacitor was fully charged. The 40-pF capacitor was used to isolate the DC high-voltage difference between the knife-edge electrode at $\sim 6.7\text{ kV}$ and the output terminal of the multistep triggering system at ground before the trigger pulse was generated. The rail-gap switch was then triggered by the multistep triggering system. Before the trigger pulse was generated, the relay controlled by a pneumatic cylinder was open so that the HV power supply was disconnected from the test bench and was not at risk of being damaged by the discharge current. Finally, the discharged currents and voltages were measured.

First, we compared the discharge characteristics of using the rail-gap switch and a three-electrode spark-gap switch. The cross section of the computer-aided design (CAD) drawing of the three-electrode spark-gap switch is shown in Fig. 11(a). All electrodes of the spark-gap switch were made of stainless steel 304. The electrodes used in the spark-gap switch are the same as those in the three-stage Marx generator. The triggering electrode is a disk with 10 mm thickness and 110 mm diameter. There is a hole at the center of the disk with a diameter of 10 mm . The gaps between the triggering electrode and each electrode were 4 mm . The case of the spark-gap switch was made of polyethylene. Similar to the rail-gap switch and the three-stage Marx generator, the spark-gap switch was filled with unpressurized-flowing dry air. The case is air-tight by using an o-ring so that the case can be pressurized for higher working voltage. The three-electrode spark-gap switch was triggered

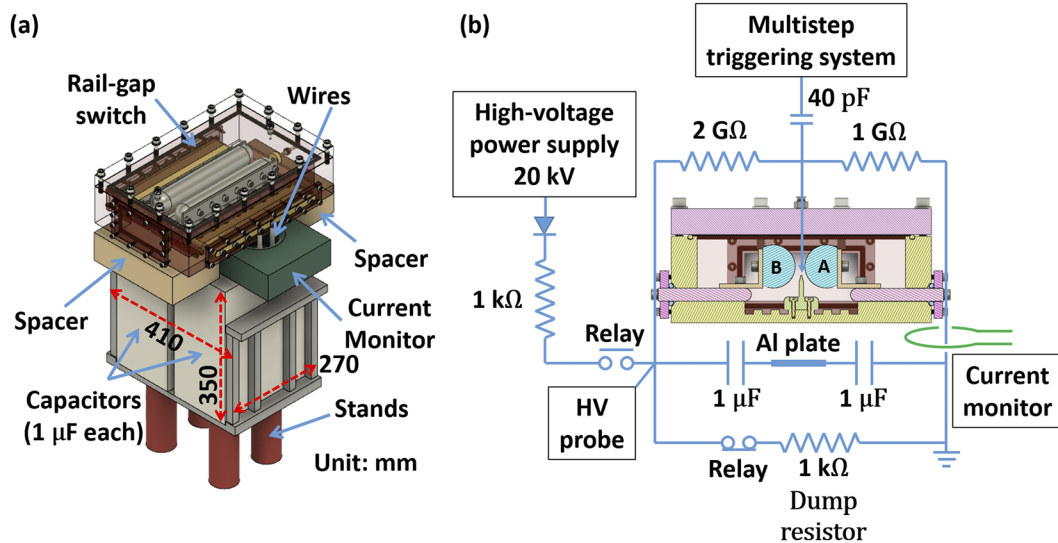


FIG. 10. (a) The CAD drawing of the test bench. (b) The circuit of the test bench. Reproduced and reprinted with permission from M.-C. Jheng, "Development of a 400 MW pulsed-power system," M.Sc. thesis, National Cheng Kung University, 2019.¹⁸

by the same multistep triggering system through the same 40-pF capacitor.

We measured the voltage across the capacitors for comparing the discharge characteristics of using the rail-gap switch and the three-electrode spark-gap switch, as shown in Fig. 11(b). The blue-solid line is from the measurement of using the three-electrode spark-gap switch. The gray-solid line is from the measurement of using the rail-gap switch. The red-dashed line is the fitted curve to the gray-solid line using the equation

$$V(t) = V_{SW0} e^{-\gamma_V(t-t_0)} \cos[\omega_V(t-t_0)], \quad (1)$$

where V_{SW0} is the amplitude of the oscillating voltage across the switch, γ_V is the damping rate of the voltage, and ω_V is the oscillation frequency. The frequency of the oscillation using the rail-gap

switch is $\omega_V = (2.270 \pm 0.010) \times 10^6$ rad/s, which is higher than that of using the three-electrode spark-gap switch, $\omega_V = (2.217 \pm 0.001) \times 10^6$ rad/s. In other words, the inductance is lower using the rail-gap switch. Most importantly, rail-gap switches will fit into the system we are building, which will be introduced by a follow-up paper, but the spark-gap switch will not.

One interesting phenomenon was that V_{SW0} was less than the charged voltage of the capacitor V_0 . It can be used to estimate the inductance of the rail-gap switch. During the discharge, some energy was used to ionize the gas in the switch. The energy was little compared to the energy stored in the capacitor. Therefore, we can neglect the lost energy for ionizing the gas in the switch. At $t = 0$, the discharge current $I(t)$ was zero. In other words, the voltage of the capacitor should be distributed across all components with finite

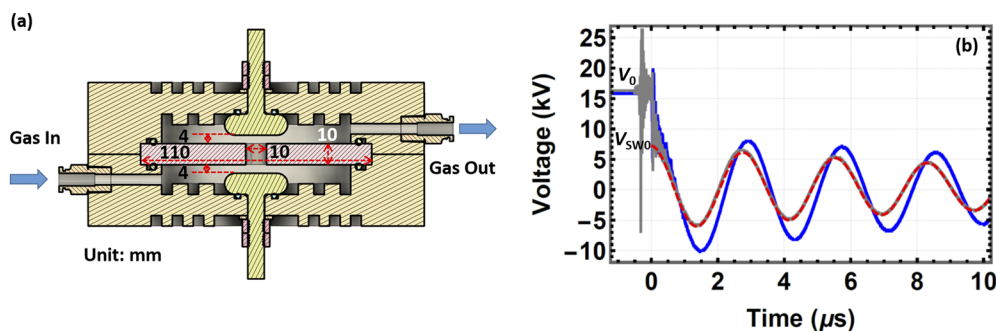


FIG. 11. (a) The CAD drawing of the three-electrode spark-gap switch we used. Reproduced and reprinted with permission from S.-H. Yang, "Developments of high voltage switches," M.Sc. thesis, National Cheng Kung University, 2018.²⁴ (b) The voltage across the capacitors during the discharge. The blue-solid line is from the discharge test using the three-electrode spark-gap switch. The gray-solid line is from the discharge test using the rail-gap switch. The red dashed line is the fitted curve of the gray-solid line using Eq. (1).

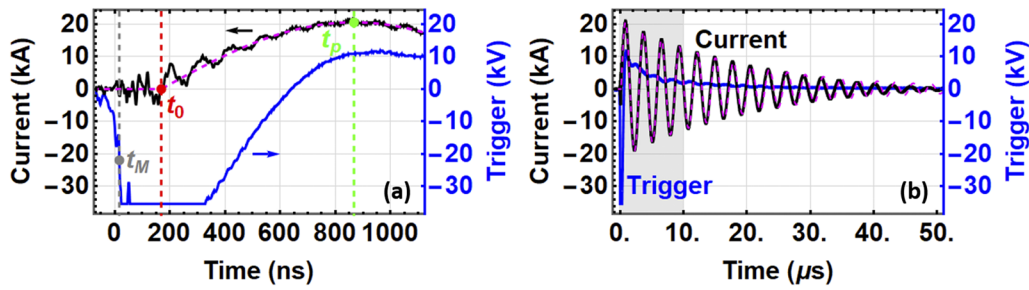


FIG. 12. The output of the discharge test. Two figures are from the same data. (a) shows the time period of -50 ns to 1100 ns. (b) shows the time period of -50 ns to 50 μ s. The black-solid line and the magenta-dashed line are the raw data and the fitted curve of the discharge current, respectively. The blue-solid line is the HV trigger pulse provided by the multistep triggering signal. Reproduced and reprinted with permission from M.-C. Jheng, "Development of a 400 MW pulsed-power system," M.Sc. thesis, National Cheng Kung University, 2019.¹⁸ The gray area in (b) shows the range of data that were used for the curve fitting using Eq. (5).

inductance, i.e.,

$$V_0 \approx V_C + V_{\text{SW-Wire}} = L_C \frac{dI}{dt} + L_{\text{SW}} \frac{dI}{dt} + L_{\text{wire}} \frac{dI}{dt}, \quad (2)$$

where

$$V_C = L_C \frac{dI}{dt} \quad \text{and} \quad V_{\text{SW-Wire}} = (L_{\text{SW}} + L_{\text{wire}}) \frac{dI}{dt}. \quad (3)$$

In other words, from the curve fitted results,

$$\frac{L_{\text{SW}} + L_{\text{wire}}}{L_{\text{tot}}} \approx \frac{V_{\text{SW0}}}{V_0} = 0.44 \pm 0.01, \quad (4)$$

calculated from nine shots.

Shown in Fig. 12 is the output of one of the shots where the output current of the capacitors is given as the black-solid line, and the HV trigger pulse provided by the multistep triggering system is given as the blue-solid line. The rail-gap switch and all cables were the load of the discharge, i.e., not a resistive load. Therefore, the discharge behaved as an underdamped RLC oscillation. The following equation is used to fit the data:

$$I(t) = \text{UnitStep}(t-t_0) I_0 e^{-\gamma(t-t_0)} \sin[\omega(t-t_0)], \quad (5)$$

where I_0 is the amplitude of the discharge current, $\gamma = -R/2L$ is the damping rate of the current, $\omega = \sqrt{\frac{1}{LC} - \left(\frac{R}{2L}\right)^2}$ is the oscillation frequency, and t_0 indicated by the red-dotted line in Fig. 12(a) is the time that the oscillation started. The function UnitStep is a unit step function, which changes from 0 to 1 at $t = t_0$. The fitted curve within the range of -200 ns to 10 μ s, which is the gray area in Fig. 12(b), is also shown in Fig. 12(a) as the magenta-dashed line. The time t_p when the peak current occurred is indicated by the green-dotted line in Fig. 12(a). With $c = 0.5$ μ F, the system inductance and resistance were obtained from the fitted γ and ω . The fitted results from 20 shots are as follows: the starting time $t_0 = 204 \pm 20$ ns, $I_0 = 21.0 \pm 0.3$ kA, $\gamma = (5.2 \pm 0.1) \times 10^4$ s⁻¹, and $\omega = (2.21 \pm 0.02) \times 10^6$ rad/s. The uncertainties were the standard deviation of the fitted numbers from all shots, i.e., shot-to-shot variation was considered. The corresponding inductance and the resistance of the system were $L = 410 \pm 6$ nH and $R = 43 \pm 1$ m Ω , respectively. From Eq. (4), $L_{\text{SW+Wire}} = 180 \pm 5$ nH. For one AWG16 high-voltage silicone wire with 50 tinned-copper cores and 100 mm length, the inductance is ~ 100 nH. Therefore, the contribution of inductance from wires was ~ 100 nH.

Therefore, the inductance of the rail-gap switch was ~ 80 nH. The peak current was $I_{\text{peak}} = 20.3 \pm 0.3$ kA at $t_p = 910 \pm 20$ ns. In addition, $t_M = 20 \pm 2$ ns indicated as the gray-dotted line in Fig. 12(a) was the time when the trigger pulse was generated. It was defined as the time when the maximum falling speed occurred. The delay between the time when the current started and the time when the triggering signal was generated was $t_{\text{delay}} \equiv t_0 - t_M = 180 \pm 20$ ns. The jitter of the delay was $\sim 10\%$ of the delay time. The delay between the time when the peak current occurred and the time when the triggering signal was generated was $t_{\text{Ip-delay}} \equiv t_p - t_M = 890 \pm 20$ ns. The rise time of the current, i.e., the first quarter period of the discharge current, is $t_{\text{rise}} \equiv t_p - t_0 = 701 \pm 5$ ns. The jitter is mainly from the activation of the rail-gap switch. Nevertheless, it is more important to have accurate peak current outputs. Therefore, the jitter of the peak current $t_{\text{Ip-delay}} \sim 2\%$ is sufficient for our future needs, which is a current pulse with a rise time of ~ 1 μ s.

We also took time-integrated images of the discharge in the rail-gap switch. Images were taken by using a commercial single-lens reflex (SLR) camera, Nikon-D750 with $f/\#$ equaled 22 and effective sensitivity of ISO50. The exposure time of the camera was 5 s, which was much longer than the discharge time that was less than 50 μ s

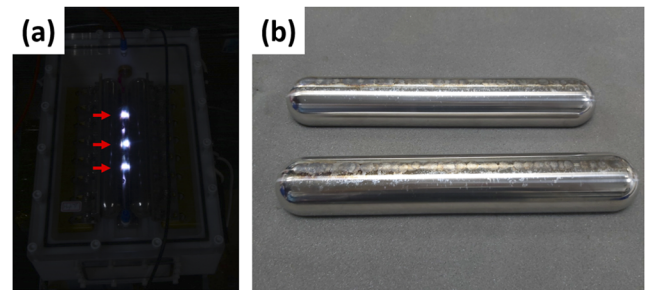


FIG. 13. (a) A time-integrated image of the rail-gap switch during the discharge. Three discharge channels pointed by red arrows were generated in this shot. The weaker flashes observed between the main channels are due to reflections from the switch bottom surface. (b) Electrodes after 30 shots. Significant damages from discharges appeared. Courtesy of Ref. 19. Reprinted with permission from C.-J. Hsieh, "Generation of plasma jets using a conical-wire array driven by a pulsed-power system," M.Sc. thesis, National Cheng Kung University, 2020.

so that the image was time integrated. Most importantly, it is much easier to achieve the synchronization between the camera and the discharge. Shown in Fig. 13(a) is one of the time-integrated images of the discharge in the rail-gap switch. A discharge channel number greater than three was obtained. In other words, the multistep triggering system performed as we expected.

Shown in Fig. 13(b) are the electrodes after 30 shots. Significant damages from the discharge occurred. Many burn marks with ~ 10 mm apart from each other indicated that the multichannel current occurred. Stainless steel 304 was used to reduce the solid debris during the discharge. However, the thermal conductivity of stainless steel (16.2 W/m K^{28}) is one order less than copper (385.0 W/m K^{29}) or brass (109.0 W/m K^{29}). The heat cannot be conducted away quickly enough leading to rough burn marks after 30 shots. Therefore, the electrodes need to be polished using sandpapers after every 30 shots. We will replace the electrodes using brass in the future because it is relatively cheap and provides better conductivity and sufficient mechanical strength.

V. SUMMARY

A rail-gap switch with a multistep triggering system was developed. The rail-gap switch was assembled from many pieces and filled with unpressurized-flowing dry air. To provide good alignments between all electrodes, the knife-edge electrode was used as the spatial reference. The rail-like electrodes were then positioned by a jig. Therefore, all electrodes parallel to each other within an angle of $\pm 5 \times 10^{-3}$ deg were achieved. Furthermore, to trigger the rail-gap switch robustly, a multistep triggering system was used. The triggering system consisted of three steps: (1) A 1.25-ms squared-optical pulse was generated by the optical trigger-pulse generator using an Arduino-nano board. The optical fiber isolated the downstream pulsed-power system and the upstream instruments. Therefore, the upstream instruments would not be damaged by the EMP generated by the downstream pulsed-power system. (2) The slow HV trigger pulse was generated using an ignition coil for a car. The primary coil of the ignition coil performed as inductive storage. A slow HV trigger pulse of less than -20 kV with a falling time and jitter of $55.5 \mu\text{s}$ and $0.4 \mu\text{s}$, respectively, was generated when the energy stored in the primary coil of the ignition coil was released and raised by the secondary coil of the ignition coil. (3) The fast HV trigger pulse was generated using a three-stage Marx generator. The first switch of the Marx generator was a controlled switch using a trigatron. The trigatron was made of a spark plug for motorcycles and triggered by the output of the slow HV trigger-pulse generator. The advantage of using the spark plug for motorcycles was that it was very robust and easily obtained. Capacitors in the Marx generator were charged to 20 kV. When all switches in the Marx generator were activated, an HV pulse less than -40 kV with a falling speed of $-6.6 \pm 0.4 \text{ kV/ns}$ was generated. The falling speed was fast enough for initiating multichannel discharges in the rail-gap switch. Finally, the rail-gap switch was tested using a test bench consisting of a capacitor bank with a capacitance of $0.5 \mu\text{F}$. The capacitor bank was also charged to 20 kV. The inductance of the rail-gap switch was ~ 80 nH obtained from discharge tests. The rail-gap switch was triggered by the multistep triggering system robustly with a delay of 180 ns. The delay between the peak current of the test bench and the trigger pulse was 890 ns with a jitter of 20 ns, i.e., $\sim 2\%$ in uncertainty. The rail-gap switch

with the multistep high-voltage triggering system is suitable for any pulsed-power systems with the current rise time in the order of $1 \mu\text{s}$.

ACKNOWLEDGMENTS

The authors are grateful to Dr. Frank J. Wessel, L-Egant Solutions, LLC, Irvine CA, USA, for valuable discussions. The authors appreciate the computational support from the Department of Aeronautics and Astronautics, National Cheng Kung University, Taiwan. This material is based on the work supported by the Ministry of Science and Technology (MOST), Taiwan, under Award No. 105-2112-M-006-014-MY3.

DATA AVAILABILITY

The data that support the findings of this study are available from the corresponding author upon reasonable request.

REFERENCES

- ¹M. K. Matzen, M. A. Sweeney, R. G. Adams, J. R. Asay, J. E. Bailey, G. R. Bennett, D. E. Bliss, D. D. Bloomquist, T. A. Brunner, R. B. Campbell, G. A. Chandler, C. A. Coverdale, M. E. Cuneo, J.-P. Davis, C. Deeney, M. P. Desjarlais, G. L. Donovan, C. J. Garasi, T. A. Haill, C. A. Hall, D. L. Hanson, M. J. Hurst, B. Jones, M. D. Knudson, R. J. Leeper, R. W. Lemke, M. G. Mazarakis, D. H. McDaniel, T. A. Mehlhorn, T. J. Nash, C. L. Olson, J. L. Porter, P. K. Rambo, S. E. Rosenthal, G. A. Rochau, L. E. Ruggles, C. L. Ruiz, T. W. L. Sanford, J. F. Seamen, D. B. Sinars, S. A. Slutz, I. C. Smith, K. W. Struve, W. A. Stygar, R. A. Vesey, E. A. Weinbrecht, D. F. Wenger, and E. P. Yu, *Phys. Plasmas* **12**, 055503 (2005).
- ²J. Hammer, *J. Phys.: Conf. Ser.* **688**, 012025 (2016).
- ³M. E. Cuneo, M. C. Herrmann, D. B. Sinars, S. A. Slutz, W. A. Stygar, R. A. Vesey, A. B. Sefkow, G. A. Rochau, G. A. Chandler, J. E. Bailey, J. L. Porter, R. D. McBride, D. C. Rovang, M. G. Mazarakis, E. P. Yu, D. C. Lamppa, K. J. Peterson, C. Nakhleh, S. B. Hansen, A. J. Lopez, M. E. Savage, C. A. Jennings, M. R. Martin, R. W. Lemke, B. W. Atherton, I. C. Smith, P. K. Rambo, M. Jones, M. R. Lopez, P. J. Christenson, M. A. Sweeney, B. Jones, L. A. McPherson, E. Harding, M. R. Gomez, P. F. Knapp, T. J. Awe, R. J. Leeper, C. L. Ruiz, G. W. Cooper, K. D. Hahn, J. McKeeney, A. C. Owen, G. R. McKee, G. T. Leifste, D. J. Ampleford, E. M. Waisman, A. Harvey-Thompson, R. J. Kaye, M. H. Hess, S. E. Rosenthal, and M. K. Matzen, *IEEE Trans. Plasma Sci.* **40**, 3222 (2012).
- ⁴G. A. Rochau, J. E. Bailey, G. A. Chandler, G. Cooper, G. S. Dunham, P. W. Lake, R. J. Leeper, R. W. Lemke, T. A. Mehlhorn, A. Nikroo, K. J. Peterson, C. L. Ruiz, D. G. Schroen, S. A. Slutz, D. Steinman, W. A. Stygar, and W. Varnum, *Plasma Phys. Controlled Fusion* **49**, B591 (2007).
- ⁵J. E. Bailey, G. A. Chandler, D. Cohen, M. E. Cuneo, M. E. Foord, R. F. Heeter, D. Jobe, P. W. Lake, J. J. MacFarlane, T. J. Nash, D. S. Nielson, R. Smelser, and J. Torres, *Phys. Plasmas* **9**, 2186 (2002).
- ⁶G. A. Rochau, J. E. Bailey, Y. Maron, G. A. Chandler, G. S. Dunham, D. V. Fisher, V. I. Fisher, R. W. Lemke, J. J. MacFarlane, K. J. Peterson, D. G. Schroen, S. A. Slutz, and E. Stambulchik, *Phys. Rev. Lett.* **100**, 125004 (2008).
- ⁷R. P. Drake, *High-Energy-Density Physics* (Springer International Publishing, 2019).
- ⁸D. Ryutov, R. P. Drake, J. Kane, E. Liang, B. A. Remington, and W. M. Wood-Vasey, *Astrophys. J.* **518**, 821 (1999).
- ⁹S. A. Pikuz, T. A. Shelkovenko, and D. A. Hammer, *Plasma Phys. Rep.* **41**, 291 (2015).
- ¹⁰J. L. Giuliani, F. N. Beg, R. M. Gilgenbach, V. L. Kantsyrev, B. R. Kuske, V. V. Ivanov, and R. Presura, *IEEE Trans. Plasma Sci.* **40**, 3246 (2012).
- ¹¹P. R. Janet Lehr, *Foundations of Pulsed Power Technology* (IEEE Computer Society Press, 2017).
- ¹²G. R. Neil and R. S. Post, *Rev. Sci. Instrum.* **49**, 401 (1978).
- ¹³E. Lopez, G. Bennett, R. Bartsch, J. Cochrane, J. Griego, R. Hicks, W. Hinckley, K. Hosack, R. Kasik, A. Marquez, W. Parsons, W. Reass, M. Thompson, and

D. Casper, in *Digest of Technical Papers. 11th IEEE International Pulsed Power Conference (Cat. No. 97CH36127)* (IEEE, 1997).

¹⁴C. Grabowski, J. H. Degnan, T. Cavazos, D. G. Gale, C. Gilman, W. Sommars, T. P. Intrator, J. M. Taccetti, B. Wagenaar, R. E. Siemon, and G. A. Wurden, *IEEE Trans. Plasma Sci.* **30**, 1905 (2002).

¹⁵Z. H. Sholapurwala, in *National Power Systems Conference* (IEEE, 2004), p. 1142.

¹⁶C. Grabowski, J. H. Degnan, J. V. Parker, J. F. Camacho, S. K. Coffey, R. K. Delaney, M. T. Domonkos, T. P. Intrator, A. G. Lynn, J. McCullough, E. L. Ruden, W. Sommars, T. E. Weber, and G. A. Wurden, *IEEE Trans. Plasma Sci.* **44**, 1997 (2016).

¹⁷R. Verma, E. Mishra, K. Sagar, M. Meena, and A. Shyam, *Rev. Sci. Instrum.* **85**, 095117 (2014).

¹⁸M.-C. Jheng, "Development of a 400 MW pulsed-power system," M.Sc. thesis, National Cheng Kung University, 2019.

¹⁹C.-J. Hsieh, "Generation of plasma jets using a conical-wire array driven by a pulsed-power system," M.Sc. thesis, National Cheng Kung University, 2020.

²⁰J. C. Martin, *On Pulsed Power* (Springer US, 2013).

²¹K. R. LeChien and J. M. Gahl, *Rev. Sci. Instrum.* **75**, 174 (2004).

²²J. R. Roth, *Industrial Plasma Engineering* (Taylor & Francis Ltd., 1995).

²³COMSOL Multiphysics®, <http://www.comsol.com>, COMSOL AB, Stockholm, Sweden.

²⁴S.-H. Yang, "Developments of high voltage switches," M.Sc. thesis, National Cheng Kung University, 2018.

²⁵M.-F. Huang, "Rust remover using small pulsed-power system," M.Sc. thesis, National Cheng Kung University, 2017.

²⁶See <http://www.plusparkstar.com/> for Shanghai Pluspark Electronics Co., Ltd., China.

²⁷See <https://www.yc-capacitor.com/index.html> for Yuhchang Electric Co., Ltd., Taiwan.

²⁸See <http://asm.matweb.com/search/SpecificMaterial.asp?bassnum=mq304a> for the information about the thermal conductivity of stainless steel.

²⁹See <http://hyperphysics.phy-astr.gsu.edu/hbase/Tables/thrcn.html> for the information about the thermal conductivity of copper and brass.